Fuel type mapping with X-band SAR in military training areas for wildfire risk assessment

Alberto García-Martín,[a,c,*] Darío Domingo,[b,c] María Teresa Lamelas,[c] Juan de la Riva,[c] Francisco Escribano,[d] Antonio Luis Montealegre,[a,c] Raquel Montorio,[c] Fernando Pérez-Cabello[c]

[a] Centro Universitario de la Defensa-Academia General Militar, Ctra. de Huesca s/n, Zaragoza, Spain

[b] University of Valladolid, EiFAB-iuFOR, Campus Duques de Soria s/n, Soria, Spain

[c] University of Zaragoza, GEOFOREST-IUCA, Department of Geography and Land Management, Pedro Cerbuna 12, Zaragoza, Spain

[d] Ejército de Tierra, Mando de Adiestramiento y Doctrina, San Matías 26, Granada, Spain

Abstract. Intense firing activities at Spanish Army Training Centers create a significant wildfire risk, requiring the implementation of a specific Plan Against Forest Fires (PAFF) and an Operational Action Protocol (OAP), both of which rely on accurate fuel type maps. This study evaluates the usefulness of the backscattering coefficient provided by PAZ, the X-band SAR Spanish Ministry of Defense's first Earth observation satellite, for fuel type mapping to support wildfire management in the "San Gregorio" Training Center (Zaragoza, Spain). The methodology involved three phases: (i) processing satellite images from the first PAZ Announcement of Opportunity (AO-001); (ii) delineating field plots for correlation with satellite imagery; and (iii) classifying fuel types using multinomial logistic regression. Results indicate that PAZ images are effective for discriminating among the main fuel types (grassland, shrubland, and woodland), achieving an overall accuracy of 82.1%. However, they are not suitable for the detailed mapping of the Prometheus fuel categories, with an overall accuracy of 42.9%, primarily due to the limited penetration capabilities of the X-band.

Keywords: Wildfire, backscattering coefficient; dominant vegetation cover; Prometheus fuel types; multinomial logistic regression; Mediterranean forest.

***Alberto García-Martín**, E-mail: algarcia@unizar.es

1 Introduction

Wildfires are considered as one of the most significant disturbance factors in the natural ecosystems of Mediterranean regions[1]. Wildfire is a landscape-shaping force in the Mediterranean basin, with which societies have learned to coexist using it as a traditional management tool[2]. However, in recent decades, wildfire recurrence, magnitude and severity have increased[3,4]. One of the main causes is the heightened combustibility of vegetation masses (quantity, surface area, volume, spatial continuity and the accumulation of dead matter), as a consequence of changes in rural depopulation, agricultural structure and land use. Added to this is the great socio-environmental challenge posed by climate change, with extreme weather conditions and prolonged periods of drought[5–7]. The 2022 summer serves as a notable example of high wildfire occurrence and intensity in Spain, France and Portugal[7–9]. Specifically, the area burned in Spain in 2022 tripled compared to the average calculated in recent decades[10]. This alarming trend was also exacerbated in 2025 when the total burned area had already surpassed 338,000 ha, according to the European Forest Fire Information System (EFFIS) dataset[11].

This reality did not go unnoticed in the Spanish National Security Strategy 2021, currently in effect, which considers wildfires as one of the main risks and threats in Spain, both in terms of “Emergencies and disasters”, as well as the “Effects of climate change and degradation of the natural environment”[12].

Wildfire risk assessment, which is key for prevention and pre-extinguishment planning, integrates ignition estimation (fuel moisture, both human and natural causal factors), spread conditions (wind, fuel properties and topography) and vulnerability assessment (socio-economic and ecological)[13–17]. Specifically, the spatial assessment of wildfire risk and wildfire intensity in wildland-urban interfaces requires mapping of forest fuels key parameters[18]. Forest fuel is the only wildfire-related landscape component that can be modified through management. Therefore, it is essential to know the fuel distribution, both for wildfire risk assessment and for the design of wildfire prevention strategies[18,19].

Among human causal factors, the activities conducted at the Spanish Army's Training Centers (TC) and Maneuver and Shooting Fields (MSF) represent a significant wildfire risk. These facilities are used for essential instruction, training, and evaluation exercises with live fire to ensure mission readiness[20]. Consequently, the intense firing activity turns projectile drop zones into potent ignition sources, threatening the natural environment, military infrastructure, and personnel safety. This inherent risk has led to the mandatory implementation of a Plan Against Forest Fires (PAFF) and an Operational Action Protocol (OAP) in all TC and MSF, as stipulated by Directive 03/19 of the Chief of Staff of the Spanish Army[21].

Remote sensing plays a major role in forest fuel characterization over landscapes offering numerous benefits over field-based approaches, particularly in its ability to make cost-efficient and objective and up-to-date observations over large and inaccessible areas. As a result, remote sensing of forest fuel is an established field of research, although the collection and interpretation of remotely sensed data requires clear objectives with regard to its intended use and spatial and temporal applicability[19]. An extensive review of the scientific literature by Ref. 19 pointed out different applications of remote sensing to forest fuel attributes, with works related to fuel type mapping being ranked second with 37% of the articles reviewed. The origin of these articles was mostly from North America and, overall, Europe, because wildfire behavior models developed for these environments usually employ a fuel type classification approach (e.g. Ref. [22–27]).

A fuel type (FT) is an identifiable association of elements characterized by their shape, size, arrangement, and continuity that will exhibit characteristic wildfire behavior under defined combustion conditions[28]. Different classifications of fuel types based on Rothermel's fire propagation equations[29] can be found in the scientific literature. In the framework of the European Prometheus project[30], an attempt was made to adapt them to the particular characteristics of Mediterranean vegetation, defining seven types that take into account the height, coverage and vertical continuity of the propagating elements. Specifically, the Prometheus classification includes: agricultural and herbaceous vegetation (FT1); three shrubland types defined by increasing height: low-lying shrubs (FT2), medium- to large-sized shrubs (FT3), and tall shrubs (FT4); and three forest types differentiated by their understory structure: forests with no significant understory (FT5); forests with an understory where the gap to the main canopy is > 0.5 m (FT6); and forests where this gap is < 0.5 m (FT7).

As noted by Ref. 18, Prometheus is a fuel type classification system in Mediterranean countries, being frequently used in remote sensing literature (e.g. Ref. [27,31–35]). However, for more operational purposes, such as providing an initial approximation to support regional firefighting strategies, a simplified classification is also considered. This approach categorizes fuel types based on dominant vegetation, resulting in three main classes: grasslands, shrublands, and forests[36,37].

Optical passive remote sensing sensors (multispectral and hyperspectral) have been the most widely used for fuel type mapping. The accuracy of the fuel type maps obtained varies depending on the sensor, the statistical methods used and the characteristics of the study area, but the main problem detected lies in the inability of these sensors to estimate the height of the vegetation and to penetrate the forest canopy, thus unveiling the characteristics of the vegetation remaining under the forest canopy[18,19,38].

In contrast, LiDAR (Light Detection and Ranging) and SAR (Synthetic Aperture Radar) active remote sensing sensors are shown to be suitable for forest structure characterization, by passing the aforementioned restrictions of optical passive sensors[39–41]. Focusing on LiDAR, this type of data is proven to be extremely useful in estimating vegetation height and subcanopy attributes[19] and for forest fuel characterization and mapping[18,42]. Although there are some examples using airborne LiDAR technology alone for fuel type mapping (e.g. Ref. [27,43,44]), most successful approaches are those that combine the use of this data with passive sensor imagery (e.g. Ref. [5,24,26,27,34,45–49]), with experiences using spaceborne LiDAR remaining scarce (e.g. Ref. [50,51]). However, as pointed out by Ref. 18,19, the main limitation for the use of airborne LiDAR data for mapping fuel types is its cost and its limited temporal and spatial coverage. Recently, a LiDAR-sensing unmanned aerial vehicle (UAV-LiDAR) has been evaluated to classify and map fuel types based on the Prometheus classification in Mediterranean environments with good results. Thus, although limited to local scales, UAV-LiDAR systems emerges as an ideal tool to spatialize the results to larger areas using sensors covering wider spatial scales[52].

Spaceborne SAR sensors, such as the one onboard the PAZ satellite, overcome these limitations by providing images of large territories at frequent intervals in all weather conditions, day and night[39,41]. The PAZ mission is a Spanish governmental radar mission and the first satellite of the Spanish National Earth Observation Program (PNOTS), which is operated directly by the Spanish Ministry of Defense through the INTA (National Institute for Aerospace Technology). Its objective is to cover the operational needs of security and defense and to provide services to civilian users in fields such as intelligence, treaty verification, catastrophe management, and wildfires, thereby supporting the Spanish National Security Strategy 2021, as mentioned above.

In spite of having proven that SAR images are useful for the estimation of forest parameters essential for fuel model mapping, such as biomass, tree height, tree volume, and canopy closure, the use of these active sensors for this issue is scarce[18]. Although research about forest parameters with SAR images has been developed mainly using C- and L-band due to the low penetration power of the X-band in the plant canopy[53,54], different studies have shown the sensitivity of the backscatter of this band for the characterization of vegetation cover and land cover mapping (e.g. Ref. [54–61]). Focusing on fuel types according to the dominant vegetation, X-band backscattering has proven adequate for mapping grasslands[60], discriminating shrublands[57] and identifying forests[61].

In this context, this study aims to assess the utility of X-band backscatter from the PAZ satellite for operational fuel mapping to support the PAFF and OAP at the TC "San Gregorio". To achieve this, we pursued two specific objectives:

1. Primary, operational objective: to develop and validate a baseline map of fuel types based on dominant vegetation cover (grasslands, shrublands, and forests), addressing an immediate operational need.

2. Secondary, exploratory objective: to evaluate the sensitivity and limitations of X-band backscatter for discriminating the more complex Prometheus fuel models, and to assess its potential to complement other remote sensing data (e.g., Sentinel-1/2 or Landsat) in future multi-sensor approaches.

For this, we make use, on the one hand, of the images provided by the first Announcement of Opportunity for Scientific Exploitation of the PAZ mission (AO-001) and, on the other hand, of the 10-meter resolution fuel model map of the study area obtained using airborne LiDAR and multispectral imagery by the authors in[45–47] and specific field work.

2 Materials and Methods

2.1 Study area

The study area corresponds to the TC "San Gregorio" (41º50' N, 0º57' W) (Fig. 1), which occupies an area of 33,839 ha in the central sector of the Ebro Depression, in the northeast of Spain (province of Zaragoza).

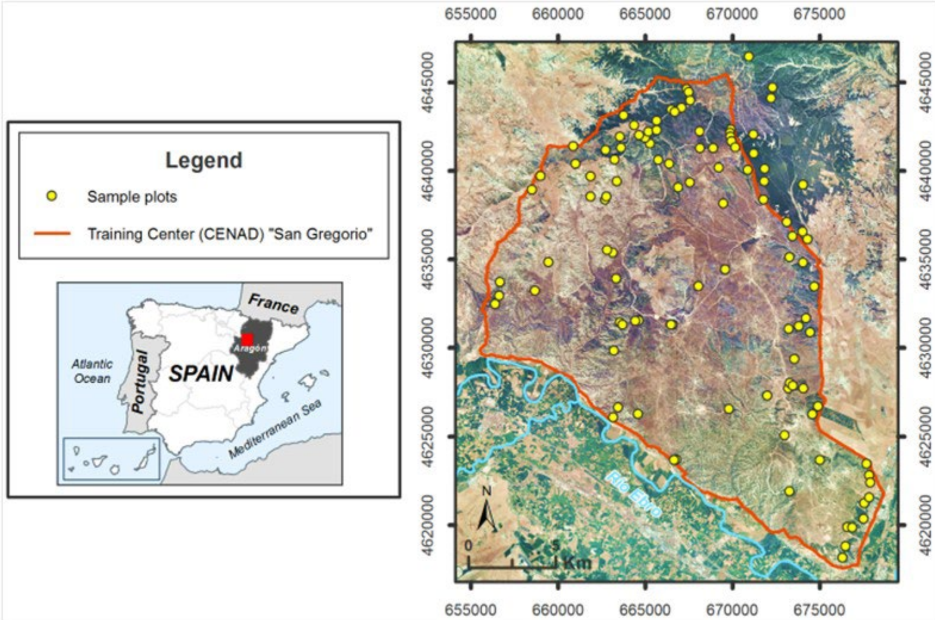

Fig. 1 Study area and localization of the field plots.

The climate of the region is Mediterranean with continental features and a semi-arid environment, characterized by irregular annual precipitation, with an average annual rainfall of 350 mm. The winters are cold, while summers are hot and dry. The area presents a hilly topography, with altitudes ranging from about 400 m to 750 m a.s.l. and has nutrient-poor gypsiferous soils.

The vegetation species are adapted to the adverse climatic and edaphic conditions of the area. Thus, the land is dominated by grass pastures and evergreen shrubs of *Quercus coccifera* L., *Juniperus oxycedrus* L., *Rosmarinus officinalis* L. and *Thymus vulgaris* L. Mono-specific stands of *Pinus halepensis* Mill., mainly concentrated in the north extreme and in discontinuous stands of varying sizes along the east-southeast boundary, occupies approximately 8,200 ha and constitutes the dominant tree strata. Most of these pine stands are semi-natural, although some of those located in the east-southeast part were planted forty years ago.

2.2 PAZ images and processing

The images captured over the study area were provided by the INTA in the context of the First Announcement of Opportunity for Scientific Exploitation of the PAZ mission[62], through the AO-001-040 project. The PAZ satellite is equipped with an X-band Synthetic Aperture Radar (SAR) instrument operating at a center frequency of 9.65 GHz (3 cm wavelength). As part of the same constellation as TerraSAR-X and TanDEM-X, it shares similar platform and instrument characteristics, ensuring high-quality data[63].

PAZ offers four Level 1B product processing variants, which maintain full compatibility with TerraSAR-X products[63]. The images used in this study were acquired in ScanSAR (SC) mode and processed as Multi Look Ground Range Detected (MGD) products. ScanSAR is designed for wide area surveillance, providing a large scene size of 100 x 150 km with a typical azimuth resolution of 18.5 m, operating with a single polarization (HH, HV, or VV) over a range of incidence angles from 20° to 45°. The MGD processing level provides magnitude-detected data projected to ground range using the WGS84 ellipsoid, which effectively reduces speckle noise and is well-suited for thematic classification[64]. The sensor features a high absolute radiometric accuracy of 0.57 dB, ensuring the quality and reliability of the backscatter measurements used in our analysis. Table 1 shows the polarization and acquisition dates of the six images used in this work.

Table 1 Acquisition dates and polarization of the PAZ images.

Acquisition date	Polarization
2020/07/06	HH
2020/07/17	HV
2020/07/28	VV
2020/08/08	HH
2020/08/19	HV
2020/08/30	VV

Given the varied topography of the study area, a critical step was to correct for terrain-induced radiometric distortions. Therefore, we applied a processing chain to normalize the backscatter coefficient to the area illuminated by the sensor, obtaining Gamma Naught ($\gamma 0$), as recommended by Ref. [65]. All processing was performed using the ESA SNAP software package (https://earth.esa.int/eogateway/tools/snap). The workflow began with the radiometric calibration of the raw data to obtain the radar brightness coefficient, Beta Naught ($\beta 0$). This was followed by a spatial multilooking step, using a 3×3 window (range × azimuth), to reduce speckle and generate an approximately square pixel with a spatial resolution of 24.75 m. Next, to correct for radiometric distortions caused by the terrain, Radiometric Terrain Flattening method was applied using the Flattening Gamma method[65] and the SRTM 1 Arc-Second Digital Elevation Model (DEM). Afterward, the images were geocoded using Geometric Terrain Correction with the Range-Doppler method, employing the same DEM to ensure geometric accuracy. Finally, a Lee speckle filter with a 3×3 kernel was applied to the terrain-corrected γ0 image to further reduce residual speckle noise, and the backscatter coefficient was then converted from linear scale to logarithmic scale and expressed in decibels (dB).

According to Ref. [66], averaging multiple co-registered SAR images is an effective method for speckle reduction, provided the scene remains stable across acquisitions. We validated this assumption of scene stability for our study period (August-September 2020) based on two key observations: (i) field work conducted concurrently with the image acquisitions revealed no significant phenological changes or disturbances in the study area and, consequently, no change between fuel types, and (ii) the temporal correlation between the individual images for each polarization was consistently high ($r > 0.8$). Given this demonstrated stability, an average image for each polarization was generated by combining the two acquisitions, enabling multitemporal multilooking and reduce residual speckle noise. Consequently, the three resulting average images were used for the subsequent statistical analysis.

2.3 Field data

The objective of this phase was to establish a ground-truth dataset to train and validate the two classification schemes defined in this study: (i) the baseline map of dominant vegetation cover and (ii) the Prometheus fuel types. To ensure that the collected data would be reliable for both analyses, the field sampling strategy was designed based on the Prometheus classification, given its more detailed and restrictive nature.

Field data acquisition was divided into two sub-phases: (i) the location and delimitation of 50 m radius plots based on a previous 10 m resolution Prometheus classification fuel type map of the study area obtained by the authors using airborne LiDAR and multispectral data (see Ref. 45-47); and (ii) field work conducted between August and September 2020 (concurrent with SAR image acquisition) to verify in situ the correspondence of each plot with the fuel model pre-assigned in the first sub-phase (Figure 2). To ensure plot suitability for digital classification models, the following requirements were followed: (i) a sufficient number of all Prometheus fuel type categories; (ii) homogeneity of fuel type within the 50 m radius plot; (iii) representativeness of slopes and topographic orientations in the study area; and (iv) accessibility to verify in situ whether the fuel type assigned by the reference cartography in Ref. 45-47 was correct. A Leica VIVA®

GS15 CS10 GNSS real-time kinematic Global Positioning System instrument was used to locate the centroids of the plots.

A final set of 113 plots was established (Figure 1; Table 2), which constitutes the ground truth for this study. On the one hand, these plots were grouped according to the Dominant Vegetation Cover (DVC) classification, resulting in four main categories: Bare soil (11 plots), DVC1 Grasslands (11 plots), DVC2 Shrublands (46 plots), and DVC3 Forest (45 plots). The number of plots for bare soil and grasslands categories were considered appropriate for the analysis, as these cover types are expected to have a simpler and more easily characterizable radiometric responses compared to the more structurally complex shrubland and forest classes. On the other hand, the plots were grouped following the Prometheus model, noting that Fuel Type 6 (FT6) was excluded from the dataset due to its limited representation in the study area.

Table 2 Fuel types description according to Prometheus classification (FT) and dominant vegetation cover (DVC) baseline map.

<table>
<tr><th>Prometheus fuel type (FT) description</th><th>Nº of plots</th><th>Dominant vegetation cover (DVC) description</th><th>Nº of plots</th></tr>
<tr><td>Bare soil</td><td>11</td><td>Bare soil</td><td>11</td></tr>
<tr><td>FT1. Agricultural and herbaceous vegetation. Grass > 60%</td><td>11</td><td>DVC1. Grasslands. Fine or light fuels, diameter <5 mm. Grass > 60%.</td><td>11</td></tr>
<tr><td>FT2. Grasslands, low-lying shrubs (0.30-0.60 m) with 30-40% of herbs. Shrub cover > 60%; Tree cover < 50%.</td><td>24</td><td rowspan="3">DVC2. Shrublands. Medium fuels, diameter between 5 and 75 mm. Shrub cover > 60%; Tree cover < 50%.</td><td rowspan="3">46</td></tr>
<tr><td>FT3. Medium- to large-sized shrubs (0.60-2.0 m), as well as young trees (> 4 m). Shrub cover > 60%; Tree cover < 50%.</td><td>14</td></tr>
<tr><td>FT4. Tall shrubs (2.0-4.0 m) and young trees (> 4 m). Shrub cover > 60%; Tree cover < 50%.</td><td>8</td></tr>
<tr><td>FT5. Forest areas (> 4 m) with no understory. Tree cover > 50%; Shrub cover < 30%.</td><td>24</td><td rowspan="3">DVC3. Forest. coarse or heavy fuels, diameter >75 mm. Tree cover > 50%.</td><td rowspan="3">45</td></tr>
<tr><td>FT6. Forest areas (> 4 m) where the mean height difference between the tree canopy and surface fuel layer is > 0.5 m. Tree cover > 50%; Shrub cover > 30%.</td><td>2</td></tr>
<tr><td>FT7. Forest areas (> 4 m) where the mean height difference between the tree canopy and surface fuel layer is < 0.5 m. Tree cover > 50%; Shrub cover > 30%.</td><td>19</td></tr>
<tr><td>Total nº of plots</td><td>113</td><td></td><td>113</td></tr>
</table>

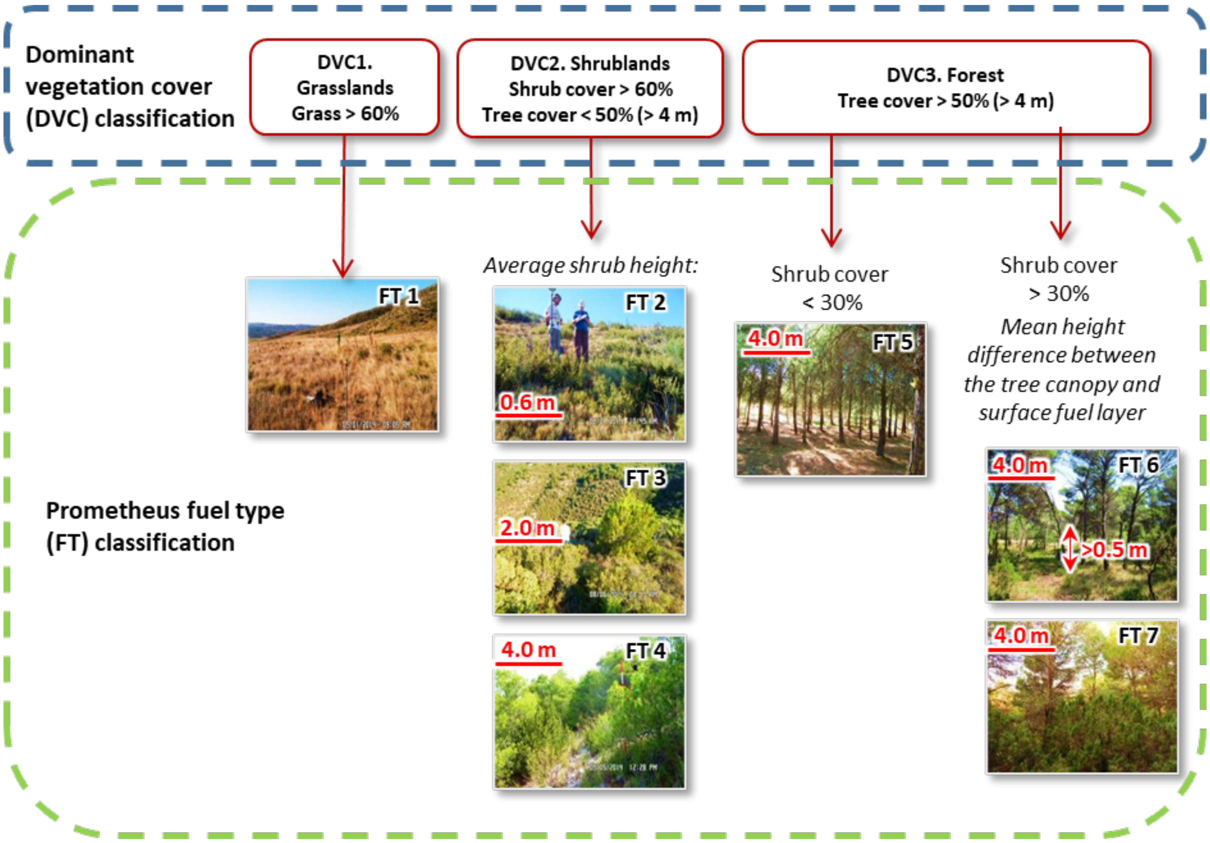

Fig. 2 Field work conducted to verify in situ the correspondence of each plot with the fuel model pre-assigned in the first sub-phase.

2.4 Fuel type classification and model validation

To perform fuel type digital classification and obtain a cartography of the study area, the radiometric value corresponding to the central pixel of each plot was extracted from the average images calculated for each polarization.

Prior to the implementation of the digital classification, an exploratory statistical analysis was conducted to investigate the relationships between the PAZ backscatter data and the fuel type categories. This preliminary analysis was essential to assess the potential separability of the classes within both the dominant vegetation cover and the Prometheus classification schemes. The analysis was structured in two main parts.

First, to quantify the strength and direction of the monotonic relationship between the backscatter values and the ordinal fuel type categories, the non-parametric Spearman's rank correlation coefficient (ρ) was calculated. This test was selected due to its robustness and because it does not assume a linear relationship between the variables, which is often the case with complex interactions between SAR signals and vegetation structure[39,67]. Second, to determine whether statistically significant differences existed between the median backscatter values of the fuel categories in each of the two classification schemes, the Kruskal-Wallis non-parametric test was applied. This test was chosen as it does not assume a normal distribution of the data, a common characteristic of SAR imagery[39,67]. A significant result from the Kruskal-Wallis test ($p < 0.05$) indicates that at least one fuel category differs from the others. To identify which specific pairs of categories were significantly different from each other, a Dunn's post-hoc test with a Bonferroni correction was subsequently performed. This detailed pairwise analysis is crucial for understanding which fuel types are likely to be confused during the classification and for evaluating the intrinsic sensitivity of the X-band backscatter to the subtle structural differences defined by the Prometheus models. All exploratory statistical analyses were conducted in the R programming environment. Spearman's rank correlation and the Kruskal-Wallis test were calculated using functions from the base 'stats' package. The Dunn's post-hoc test for pairwise comparisons was performed using the Dunn Test function from the 'FSA' package[68].

Following the exploratory analysis, the digital classification of fuel types was performed using multinomial logistic regression. This statistical method was chosen to model the probability of a given pixel belonging to one of the defined fuel type categories based on its PAZ backscatter values as explanatory variables[69]. This approach was selected over non-parametric machine learning algorithms, such as Random Forest (RF) and Support Vector Machine (SVM), due to its robustness with small to medium-sized datasets. While powerful, algorithms like RF and SVM are highly flexible and data-driven, which increases the risk of overfitting when trained on a limited number of samples[70], as was the case in this study (113 plots). Overfitting occurs when a model learns the training data, including its statistical noise, so perfectly that it fails to generalize to new, unseen data. In contrast, multinomial logistic regression is a parametric model that is less prone to this issue. Its underlying assumptions provide a form of regularization, leading to simpler, more generalized models that are more reliable when data is scarce[71]. The multinomial logistic regression model was implemented in the R programming environment. The model was fitted using the “multinom” function from the “nnet” package[72], while model validation and the calculation of performance metrics, such as the confusion matrix, were conducted using the “Caret” package[73]. To build and evaluate the model, the field plots were partitioned using a stratified random split, allocating 75% of the data for training (n=85) and reserving the remaining 25% for independent validation (n=28).

3 Results

3.1. Spearman correlation

Table 3 presents the Spearman correlation analysis between the averaged PAZ backscatter values and the fuel type categories for both the Dominant Vegetation Cover (DVC) and the Prometheus (FT) classification schemes. The results for both schemes indicate that the HV polarization exhibits the strongest relationship with the fuel types, showing a moderate and positive correlation for both the DVC classification ($\rho = 0.496$) and the more detailed FT classification ($\rho = 0.513$). In contrast, the co-polarized bands (HH and VV) showed very weak correlations for both classification systems ($\rho < 0.13$). It is important to note that all reported correlations in the analysis were statistically significant ($p < 0.05$). This finding is consistent with the scientific literature, which widely recognizes that cross-polarization (HV) is more sensitive to volume scattering from vegetation canopies than co-polarized bands[39,67].

Table 3 Spearman's rank correlation coefficient between PAZ averaged images and fuel type categories. All the relationships were statistically significant ($p < 0.05$).

PAZ averaged images	Spearman correlation DVC fuel types	Spearman correlation Prometheus fuel types
HH	0,100	0.123
HV	0.496	0.513
VV	0.060	0.083

3.2 Analysis of Fuel Type Separability

The Kruskal-Wallis test indicated that for both the Dominant Vegetation Cover (DVC) and the Prometheus (FT) classification schemes, the backscatter values of all three PAZ polarizations (HH, HV, and VV) showed statistically significant differences among the fuel type categories ($p < 0.05$) (Table 4). This confirms that the X-band signal is sensitive to the structural differences between the defined fuel types. To identify which specific classes could be distinguished, a Dunn's post-hoc test was subsequently applied.

For the broader DVC classification, the Dunn's test revealed a high degree of separability among the categories. Table 5 presents pairwise comparisons between the categories that were statistically significant ($p < 0.05$). The HV polarization was the most versatile, successfully distinguishing four of the six possible pairs. It was able to separate Grasslands (DVC1) from both Shrublands (DVC2) and Forests (DVC3), and also distinguished both Shrublands and Forests from Bare soil. The co-polarized bands also provided critical information. Both HH and VV polarizations effectively separated Grasslands (DVC1) from Bare soil. Crucially, the VV polarization was the only one capable of significantly distinguishing between Shrublands (DVC2) and Forests (DVC3), a key separation for fuel type mapping. In summary, by combining the information from all three polarizations, all pairs of DVC categories were found to be statistically separable, indicating a strong potential for successful classification at this broader thematic level.

The analysis of the more detailed Prometheus types provided deeper insights into the specific capabilities and limitations of the X-band backscatter. The results from the Dunn's test showed that the HV polarization was again the most effective, identifying seven statistically significant pairs of fuel models ($p < 0.05$) (Table 5). Notable separations were achieved between fuel types with large differences in vegetation structure and biomass. For instance, forest with no understory (FT5) was significantly different from all three shrubland categories (FT2, FT3, and FT4), indicating that the sensor can clearly distinguish between a closed-canopy forest and open shrublands. Similarly, forest with high vertical continuity (FT7) was separable from the lower-stature shrub classes (FT2 and FT3). This suggests that volume scattering captured by the HV channel is highly sensitive to the presence of a dense forest canopy and understory. Conversely, the analysis also highlighted significant confusion between structurally similar classes. A critical challenge was the lack of separability within the shrubland continuum; no significant differences were found between low-lying shrubs (FT2), medium-sized shrubs (FT3), and tall shrubs (FT4). This indicates that while the X-band can differentiate shrublands from forests, it struggles to resolve finer-scale differences in shrub height and density. Similarly, the two main forest types, FT5 (no understory) and FT7 (with understory), could not be statistically separated from each other, suggesting that the X-band signal has difficulty penetrating the main forest canopy to characterize the understory structure—a known limitation of this wavelength. Finally, the herbaceous category (FT1) could not be reliably distinguished from bare soil or the low-shrub class (FT2).

Table 4 Results from Kruskal-Wallis test for DVC and Prometheus FT. All variables were statistically significant ($p\text{-value} < 0.05$)

PAZ averaged images	Chi-square coefficient DVC fuel types	Chi-square coefficient Prometheus fuel types
HH	36.053	45.545
HV	39.090	44.022
VV	27.521	37.429

Table 5 Results from Dunn's test to distinguish categories DVC and Prometheus fuel types. All pairwise comparisons between the categories were statistically significant ($p < 0.05$)

DVC fuel types		Prometheus fuel types	
PAZ averaged images	**Comparison**	**PAZ averaged images**	**Comparison**
HH	Bare soil - DVC1 Bare soil - DVC2 Bare soil - DVC3 DVC2 - DVC3	HH	Bare soil - FT1 Bare soil - FT2 Bare soil - FT3 FT2 - FT3 Bare soil - FT4 Bare soil - FT5 FT3 - FT5 Bare soil - FT7 FT3 - FT7
HV	Bare soil - DVC1 Bare soil - DVC2 DVC1 - DVC2 Bare soil - DVC3 DVC1 - DVC3	HV	Bare soil - FT2 Bare soil - FT3 FT1 - FT3 FT2 - FT3 Bare soil - FT4 Bare soil - FT5 FT1 - FT5 Bare soil - FT7 FT1 - FT7
VV	Bare soil - DVC1 Bare soil - DVC2 Bare soil - DVC3 DVC2 - DVC3	VV	Bare soil - FT1 Bare soil - FT2 Bare soil - FT3 Bare soil - FT4 FT2 - FT5 FT3 - FT5 Bare soil - FT7

3.3. Fuel type classification

The multinomial logistic regression model, utilizing the three PAZ polarization backscatter values (HH, HV, and VV) as predictors, was trained and validated to classify the Dominant Vegetation Cover (DVC) categories. The model demonstrated strong predictive performance on the independent test dataset, achieving an Overall Accuracy of 82.1% and a Cohen's Kappa coefficient of 0.72.

A detailed analysis of the model's performance is provided by the confusion matrix (Table 6). The model performed exceptionally well in identifying Bare soil, classifying all test plots for this category correctly (100% Producer's and User's Accuracy). The classification of the forest (DVC3) category was also highly proficient, achieving a producer's accuracy of 90.9%. The primary source of classification error was the significant confusion involving the grasslands (DVC1) and shrublands (DVC2) categories. A notable challenge for the model was the identification of grasslands, with two of the three test plots being misclassified as shrublands. This resulted in a low producer's accuracy of 33.3% for the grasslands class. Consequently, although the shrublands class was well-identified (81.8% producer's accuracy), it incorrectly absorbed plots from both grasslands and, to a lesser extent, forest, which lowered its user's accuracy to 75%. This pattern suggests that, although statistically separable, the spectral signature of grasslands in the X-band is frequently confused with that of low-shrub formations, posing a challenge for the classification model.

Table 6 Confusion matrix and per-class accuracy metrics from the multinomial logistic regression model for the Dominant Vegetation Cover (DVC) classification. The results were obtained on the independent test dataset (n=28).

	Bare soil	**Grassland (DVC1)**	**Shrubland (DVC2)**	**Forest (DVC3)**	**User's Accuracy**	**Producer's Accuracy**
Bare soil	100.00	0.00	0.00	0.00	100.00	100.00
Grassland **(DVC1)**	0.00	100.00	0.00	0.00	100.00	33.33
Shrubland **(DVC2)**	0.00	16.67	75.00	8.33	75.00	81.82
Forest **(DVC3)**	0.00	0.00	16.67	83.33	83.33	90.91

When applied to the more detailed Prometheus fuel type classification, the multinomial logistic regression model showed a considerable decrease in performance. The model achieved an overall accuracy of 42.9% on the independent test dataset, with a Cohen's Kappa coefficient of 0.31. These metrics indicate that while the model performs better than random chance, it faces significant challenges in distinguishing between these finer-scale fuel categories.

The confusion matrix (Table 7) provides a detailed view of the model's performance and highlights the specific areas of confusion, which align with the findings from the exploratory separability analysis. The model was successful at identifying broad structural groups. For instance, bare soil and herbaceous vegetation (FT1) were identified with moderate success. The classification of forest areas (FT5) also showed some proficiency, achieving the highest producer's accuracy (66.7%) among the vegetated classes. However, the model exhibited significant confusion between structurally similar fuel types, with three primary patterns of error being observed. First, there was considerable confusion within the shrubland continuum, where the model struggled to differentiate between the various shrub classes. Medium- to large-sized shrubs (FT3) and tall shrubs (FT4) were not correctly identified at all (0% producer's accuracy), being frequently misclassified as other shrub types or even forest. A similar pattern occurred within the forest types, as the model had great difficulty separating forest with no understory (FT5) from forest with high vertical continuity (FT7), with significant misclassifications occurring between these two categories. Finally, the model often confused herbaceous vegetation (FT1) with low-lying shrubs (FT2) and even bare soil, indicating that the X-band signal struggles to resolve the subtle differences between these sparse fuel types. In summary, these results suggest that while the PAZ X-band data can effectively separate broad categories like forests from shrublands, its sensitivity is limited for finer-scale classification within these groups.

Table 7 Confusion matrix and per-class accuracy metrics from the multinomial logistic regression model for the Prometheus classification. The results were obtained on the independent test dataset (n=28).

	Bare soil	**FT1**	**FT2**	**FT3**	**FT4**	**FT5**	**FT7**	**User's Accuracy**	**Producer's Accuracy**
Bare soil	100.00	0.00	0.00	0.00	0.00	0.00	0.00	100.00	66.67
FT1	33.33	33.33	0.00	33.33	0.00	0.00	0.00	33.33	33.33
FT2	0.00	25.00	37.50	12.50	12.50	12.50	0.00	37.50	50.00
FT3	0.00	0.00	75.00	0.00	0.00	0.00	25.00	0.00	0.00
FT4	-	-	-	-	-	-	-	-	0.00
FT5	0.00	0.00	0.00	0.00	14.29	57.14	28.57	57.14	66.67
FT7	0.00	0.00	0.00	25.00	0.00	25.00	50.00	50.00	40.00

Based on these findings, a clear difference in performance emerged between the two classification schemes. The model based on the Dominant Vegetation Cover (DVC) categories achieved an overall accuracy of 82.1% and demonstrated a robust capability to distinguish between the broad fuel classes. In contrast, the model trained on the more detailed Prometheus fuel types, while informative, yielded a modest accuracy (42.9%) and showed significant confusion between structurally similar categories. Given this performance gap, it was concluded that the Prometheus-level model did not possess the necessary reliability for producing an accurate thematic map. Therefore, the final fuel type map of the study area was generated using exclusively the logistic regression model fitted with the Dominant Vegetation Cover (DVC) categories (Figure 3).

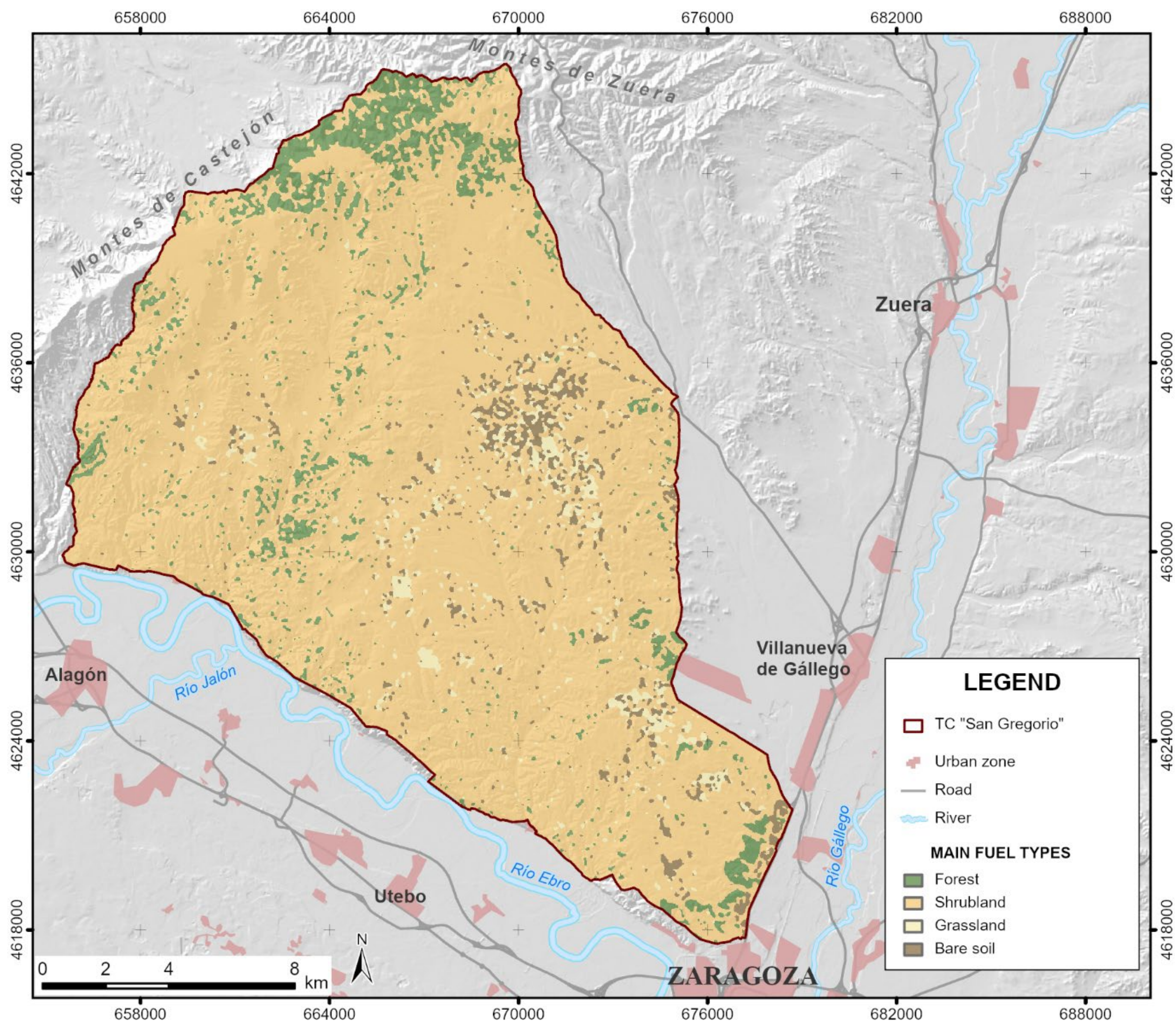

Fig. 3 Map of the dominant vegetation cover (DVC) fuel types in the TC "San Gregorio".

4. Discussion

Fuel type maps provide essential information for forest managers to support prevention, wildfire management and wildfire risk modeling[18,19,33]. This cartography is particularly relevant in forested areas affected by wildfires[74] and where there is a potential risk of wildfires due to the activities conducted in the area[75]. The TC and MSF utilized by the Spanish Army satisfy the aforementioned dual criterion as they are employed for the purpose of live ammunition firing practice and are situated predominantly in the Mediterranean region, distinguished by elevated aridity and combustibility. Our study illustrates the utility of the X-band PAZ satellite for characterizing vegetation structure in Mediterranean environments. As the first satellite of the Spanish National Earth Observation Program (PNOTS), the PAZ mission is an operational asset of the Spanish Ministry of Defense, designed primarily to cover security and defense needs. However, its capabilities also extend to critical civilian applications, including catastrophe and wildfire management. This dual-use nature makes it a uniquely suitable instrument for this study, demonstrating how a strategic defense asset can be leveraged to support the specific regulations developed by the Spanish Army to prevent and combat wildfires on lands under its jurisdiction.

The exploratory statistical analysis confirmed the sensitivity of the PAZ X-band backscatter to the structural attributes of forest fuel types. Spearman's correlation analysis showed that the HV cross-polarization exhibited the strongest relationships with both classification schemes ($\rho \approx 0.5$). This result is consistent with the well-documented sensitivity of cross-polarization to volume scattering from vegetation canopies, in contrast to the stronger surface contributions in co-polarized channels[39,67,76,77]. Its effectiveness stems from its sensitivity to various vegetation parameters including biomass (e.g. Ref. [53,54,78,79]), vegetation water content (e.g. Ref. [79–81]) and structural properties (e.g. Ref. [82–84]). Likewise, the Dunn's post-hoc test revealed that at the broader Dominant Vegetation Cover (DVC) level, all fuel categories were statistically separable, providing a strong a priori justification for classification. Conversely, the more detailed Prometheus scheme exposed the intrinsic limitations of X-band SAR for resolving subtle structural differences, particularly within the shrubland continuum and between forest types with or without understory, foreshadowing the challenges later observed in classification accuracy.

These pre-classification insights were directly reflected in the performance of the multinomial logistic regression model. For the DVC classification, the model achieved a high overall accuracy of 82.1% (Kappa = 0.72), indicating robust discrimination between bare soil, grasslands, shrublands, and forests. This result is particularly noteworthy as it was achieved using only a single SAR-based approach, which is independent of cloud cover and illumination conditions, highlighting its suitability for operational mapping. The main source of error was the misclassification of grasslands as shrublands. This confusion likely reflects a known limitation of X-band backscatter: its restricted dynamic range when characterizing vegetation. Previous studies have shown that the sensor signal tends to saturate over dense grasslands and shrublands, reducing its ability to capture structural differences at high biomass levels[57,85]. The sensor is also relatively insensitive to subtle variations in low-biomass formations. As a result, sparse grasslands and low-lying shrubs produce similarly weak backscatter responses, making them difficult to distinguish and leading to systematic misclassification between these two categories. Furthermore, from a statistical standpoint, the distinction between the grassland and shrubland categories may have been poorly characterized in our work due to the imbalanced number of plots in each class (11 and 46, respectively). To better resolve this confusion, it would be necessary to increase the sample size for the grassland category in future fieldwork.

Limitations of X-band SAR for resolving subtle structural differences—particularly within the shrubland continuum and between forest types with or without an understory—have been highlighted in several studies. For example, in forested environments, the shallow penetration depth of X-band hampers the detection of sub-canopy layers, making it difficult to distinguish forests with and without understory[86]. More recent analyses confirm this limitation: TanDEM-X data show restricted sensitivity to sub-canopy topography due to the limited penetration of X-band through dense canopies[87], and X-band inversion algorithms demonstrate reduced accuracy in stratified stands where understory is present[88]. Together, these findings corroborate that while X-band SAR is highly effective for broad vegetation mapping, it lacks the structural sensitivity required for finer differentiation within shrublands and between forest structural types.

By comparison, our work has achieved similar accuracies for Prometheus in Mediterranean regions in approaches that have been used a single data sensor (e.g. Ref. [27]), but lower than approaches that relied on multi-sensor fusion approaches—integrating LiDAR to capture vertical structure and multispectral and/or SAR data to characterize vegetation composition and vigor (e.g. Ref. [5,89]). Focusing on our own previous experiences in the study area, the confusion matrix hit rates represent about 59% of those obtained with SPOT-5 and low-density Airborne Laser Scanner (ALS) data[45–47], 47% of those achieved with the Discrete Anisotropic Radiative Transfer (DART) model used to replicate low-density small-footprint LiDAR measurements[6] and 51% of those obtained when combining Landsat and GEDI data[51]. It should be noted, however, that datasets of this last study are not continuous, but discretized in circular diameter traces.

Finally, the use of multinomial logistic regression instead of more complex machine learning algorithms such as Support Vector Machines (SVM) or Random Forest (RF) was a deliberate methodological choice. While non-parametric methods have been reported to achieve high accuracies in some fuel mapping studies, they are highly data-demanding and prone to overfitting with small to medium-sized samples[70]. For example, Arellano-Pérez et al.[90] observed that the RF algorithm overestimated data from small sample plots (123 field plots) when modelling surface and canopy fuel characteristics with Sentinel-2A data and Hu et al.[91] observed this phenomenon when predicting forest stand volume with Sentinel-2A imagery and 459 field plots. Our previous studies also showed that overfitting was produced in RF when predicting different forest attributes when the field sample is not very large (192 plots Domingo et al.[92] and Domingo et al.[93]), although in Domingo et al.[5] SVM had good accuracy to classify Prometheus fuel types using 136 plots as ground-truth.

5 Conclusions

This study aimed to assess the utility of X-band backscatter from the PAZ satellite for operational fuel mapping to support the PAFF and OAP at the TC "San Gregorio". This general objective was motivated by the critical need to improve wildfire risk management in highly fire prone areas, such as military training areas.

The two specific objectives were addressed with different levels of success. First, the study sought to develop and validate a baseline map of fuel types based on dominant vegetation cover (grasslands, shrublands, and forests), addressing an immediate operational need. This objective was successfully achieved: all three SAR polarizations were sensitive to vegetation structure, with HV cross-polarization performing best. Using a multinomial logistic regression model, a reliable map of dominant vegetation cover was produced, achieving high overall accuracy (82.1%) and effectively distinguishing between bare soil, grasslands, shrublands, and forests. Second, the study aimed to conduct an exploratory analysis of X-band sensitivity for discriminating the more complex Prometheus fuel types, assessing its potential to complement other remote sensing data. The analysis revealed limitations: while broad structural differences were detectable, the classification of detailed Prometheus fuel types reached only 42.9% accuracy. This highlights that PAZ X-band imagery alone is insufficient for fine-scale fuel mapping but remains valuable for strategic, broad-level applications.

Finally, the sensitivity of HV polarization suggests that future work could explore synergistic use with other data sources, including longer-wavelength radar (C and L bands), LiDAR (UAV, airborne, or satellite), and medium- to high-resolution optical imagery (e.g., Sentinel-2). Advanced PolSAR and InSAR techniques applied to PAZ data could further enhance biomass and vegetation structure characterization, improving fuel type classification in more detailed multi-sensor approaches.

Disclosures

The authors declare that there are no financial interests. commercial affiliations. or other potential conflicts of interest that could have influenced the objectivity of this research or the writing of this paper.

Code and Data Availability

The data that support the findings of this article are not publicly available due to security and defense concerns. They can be requested from the author at algarcia@unizar.es.

Acknowledgments

This research was funded by the projects "AO-001-040" of the National Institute for Aerospace Technology (INTA), "FUELPAZ" [2019-12] of the Centro Universitario de la Defensa of the Academia General Militar (CUD-AGM), and "PaF" [PID2020-118886RB-I00] of the Ministerio de Ciencia, Innovación y Universidades; and by the Government of Aragon [Geoforest S51_23R, FEDER "Construyendo Europa desde Aragón"]. ChatGPT 3.5. Gemini 2.5 pro and DeepL were used for the linguistic and grammatical cleaning of the text.

References

1. R. Lasaponara and A. Lanorte, "Remotely sensed characterization of forest fuel types by using satellite ASTER data," Int. J. Appl. Earth Obs. Geoinf. **9**(3), 225–234 (2007) [doi:10.1016/j.jag.2006.08.001].
2. J. G. Pausas et al., "Are wildfires a disaster in the Mediterranean basin? A review," Int. J. Wildl. Fire **17**(6), 713–723 (2008) [doi:10.1071/WF07151].
3. S. González-De Vega, J. De las Heras, and D. Moya, "Resilience of Mediterranean terrestrial ecosystems and fire severity in semiarid areas: Responses of Aleppo pine forests in the short, mid and long term," Sci. Total Environ. **573**, 1171–1177, Elsevier B.V. (2016)

[doi:10.1016/j.scitotenv.2016.03.115].

4. A. San-Miguel-Ayanz, J.; Rodrigues, M.; de Oliveira, S.S.; Pacheco, C.K.; Moreira, F.; Duguy, B.; Camia, “Land Cover Change and Fire Regime in the European Mediterranean Region,” in Post-Fire Management and Restoration of Southern European Forests. Managing Forest Ecosystems **24**, Springer, J. Moreira, F., Arianoutsou, M., Corona, P., De las Heras, Ed., p. 2208, Dordrecht (2012) [doi:10.1007/978-94-007-2208-8_2].
5. D. Domingo et al., “Fuel type classification using airborne laser scanning and sentinel 2 data in mediterranean forest affected by wildfires,” Remote Sens. **12**(21), 1–22 (2020) [doi:10.3390/rs12213660].
6. S. Revilla et al., “Assessing the potential of the dart model to discrete return lidar simulation—application to fuel type mapping,” Remote Sens. **13**(3) (2021) [doi:10.3390/rs13030342].
7. M. Rodrigues et al., “Drivers and implications of the extreme 2022 wildfire season in Southwest Europe,” Sci. Total Environ. **859**(September 2022), 160320, Elsevier B.V. (2023) [doi:10.1016/j.scitotenv.2022.160320].
8. J. San-Miguel-Ayanz et al., *Advance Report on Forest Fires in Europe, Middle East and North Africa 2022*, in Publications Office of the European Union, Luxembourg(May) (2023) [doi:10.2760/091540].
9. M. Rodrigues et al., “An empirical assessment of the potential of post-fire recovery of tree-forest communities in Mediterranean environments,” For. Ecol. Manage. **552**(November 2023) (2024) [doi:10.1016/j.foreco.2023.121587].
10. M. A. Tanase et al., “Long-term annual estimation of forest above ground biomass, canopy cover, and height from airborne and spaceborne sensors synergies in the Iberian Peninsula,” Environ. Res. **259**(May), 119432, Elsevier Inc. (2024) [doi:10.1016/j.envres.2024.119432].
11. J. R. C. (JRC) European Commission, “European Forest Fire Information System (EFFIS) dataset,” 2025, <https://effis.jrc.ec.europa.eu> (accessed 2 October 2025).
12. Presidencia del Gobierno de España, *Estrategia de Seguridad Nacional 2021*, in Ministerio de la Presidencia, Realciones con las Cortes y Memoria Democrática, G. de España, Ed., Madrid (2021).
13. E. Chuvieco et al., “Towards an Integrated Approach to Wildfire Risk Assessment: When, Where, What and How May the Landscapes Burn,” Fire **6**(5), 1–60 (2023) [doi:10.3390/fire6050215].
14. E. Chuvieco et al., “Development of a framework for fire risk assessment using remote sensing and geographic information system technologies,” Ecol. Modell. **221**(1), 46–58 (2010) [doi:10.1016/j.ecolmodel.2008.11.017].
15. A. Novo et al., “Mapping Forest Fire Risk — A Case Study in,” Remote Sens. **12** (2020).

16. M. Naderpour, H. M. Rizeei, and F. Ramezani, “Forest fire risk prediction: A spatial deep neural network-based framework,” Remote Sens. **13**(13) (2021) [doi:10.3390/rs13132513].

17. Z. Parvar, S. Saeidi, and S. Mirkarimi, “Integrating meteorological and geospatial data for forest fire risk assessment,” J. Environ. Manage. **358**(April), 120925, Elsevier Ltd (2024) [doi:10.1016/j.jenvman.2024.120925].

18. A. Abdollahi and M. Yebra, “Forest fuel type classification: Review of remote sensing techniques, constraints and future trends,” J. Environ. Manage. **342**(June), 118315, Elsevier Ltd (2023) [doi:10.1016/j.jenvman.2023.118315].

19. M. G. Gale et al., “Forest fire fuel through the lens of remote sensing: Review of approaches, challenges and future directions in the remote sensing of biotic determinants of fire behaviour,” Remote Sens. Environ. **255**(July 2020), 112282, Elsevier Inc. (2021) [doi:10.1016/j.rse.2020.112282].

20. Revista Ejército, “Centro de Adiestramiento San Gregorio,” Rev. Ejército **800**, 8–29 (2007).

21. Ministry of Defence, “Directiva 03/19: Acciones contra incendios forestales en los campos de maniobras y tiro, y otras propiedades asignadas al Ejército de Tierra,” Madrid (2019).

22. A. Alonso-Benito et al., “Pixel and object-based classification approaches for mapping forest fuel types in Tenerife Island from ASTER data,” Int. J. Wildl. Fire **22**(3), 306–317 (2013) [doi:10.1071/WF11068].

23. S. Bajocco et al., “Mapping forest fuels through vegetation phenology: The role of coarse-resolution satellite time-series,” PLoS One **10**(3), 1–14 (2015) [doi:10.1371/journal.pone.0119811].

24. M. K. Jakubowksi et al., “Predicting surface fuel models and fuel metrics using lidar and CIR imagery in a dense mixed conifer forest,” Photogramm. Eng. Remote Sens. **79**(1), 37–49 (2013).

25. A. Stefanidou et al., “Fuel type mapping using object-based image analysis of DMC and Landsat-8 OLI imagery,” Geocarto Int. **33**(10), 1064–1083 (2018) [doi:10.1080/10106049.2017.1333532].

26. M. F. Rosa and D. A. Stow, “Mapping fuels at the wildland-urban interface using colour ortho-images and LiDAR data,” Geocarto Int. **29**(5), 570–588 (2014) [doi:10.1080/10106049.2013.819040].

27. M. Huesca, D. Riaño, and S. L. Ustin, “Spectral mapping methods applied to LiDAR data: Application to fuel type mapping,” Int. J. Appl. Earth Obs. Geoinf. **74**(August 2018), 159–168 (2019) [doi:10.1016/j.jag.2018.08.020].

28. M. E. Merrill, D. F., Alexander, *Glossary of forest fire management terms*, Committee on Forest Fire Management, National Research Council of Canada., Ottawa (1987).

29. R. C. Rothermel, *A mathematical model for predicting fire spread in wildland fuels. US*

Department of Agriculture, Intermountain Forest and Range Experiment Station, 40, p. 115, US Department of Agriculture, Intermountain Forest and Range Experiment Station, Ogden (1972).

30. S. Prometheus, “Management techniques for optimization of suppression and minimization of wildfire effects. System Validation. Contract number ENV4-CT98-0716.” (1999).

31. L. Mitri, G.H.; Nader, M.; Salloum, “Fuel type mapping in the Mediterranean region of north Lebanon using object-based image analysis of aster imagery,” in Advances in Remote Sensing and GIS applications in Forest Fire Management From local to global assessments, S. San-Miguel Ayanz, J.; Gitas, I.; Camia, A.; Oliveira, Ed., pp. 39–44, European Comission (2011) [doi:10.2788/66489].

32. A. García-Cimarras, J. A. Manzanera, and R. Valbuena, “Analysis of mediterranean vegetation fuel type changes using multitemporal lidar,” Forests **12**(3), 1–16 (2021) [doi:10.3390/f12030335].

33. A. Alonso-Benito et al., “Fusion of WorldView-2 and LiDAR data to map fuel types in the Canary Islands,” Remote Sens. **8**(8) (2016) [doi:10.3390/rs8080669].

34. M. García et al., “Multispectral and LiDAR data fusion for fuel type mapping using Support Vector Machine and decision rules,” Remote Sens. Environ. **115**(6), 1369–1379, Elsevier Inc. (2011) [doi:10.1016/j.rse.2011.01.017].

35. D. Riaño et al., “Generation of fuel type maps from Landsat TM images and ancillary data in Mediterranean ecosystems,” Can. J. For. Res. **32**(8), 1301–1315 (2002) [doi:10.1139/x02-052].

36. R. Vélez Muñoz, *La defensa contra incendios forestales. Fundamentos y experiencias*, McGraw-Hill, Madrid (2009).

37. F. Aguirre, *Manual de formación de incendios forestales para cuadrillas*, Gobierno de Aragón, Zaragoza (2006).

38. L. A. Arroyo, C. Pascual, and J. A. Manzanera, “Fire models and methods to map fuel types: The role of remote sensing,” For. Ecol. Manage. **256**(6), 1239–1252 (2008) [doi:10.1016/j.foreco.2008.06.048].

39. M. L. A. Henderson, *Principles and applications of imaging radar*, John Wiley & Sons, Inc., New York (1998).

40. H.-G. Vosselman, G.; Maas, *Airborne and Terrestrial Laser Scanning; Whittles Publishing: Dunbeath, UK, 2010; p. 320.*, Whittles Publishing, Dunbeath (2010).

41. V. . A. . Campbell , J . B ., Wynne , R . H ., Thomas, *Introduction to Remote Sensing.*, Guilford Publications, New York (2022).

42. E. Marino et al., “Generation of high-resolution fuel model maps from discrete airborne laser scanner and Landsat-8 OLI: A low-cost and highly updated methodology for large areas,” Remote

Sens. Environ. **187**, 267–280, Elsevier Inc. (2016) [doi:10.1016/j.rse.2016.10.020].

43. J. R. González-Olabarria et al., “Mapping fire risk in the Model Forest of Urbión (Spain) based on airborne LiDAR measurements,” For. Ecol. Manage. **282**, 149–156 (2012) [doi:10.1016/j.foreco.2012.06.056].

44. M. T. Lamelas-Gracia, D. Riaño, and S. Ustin, “A LiDAR signature library simulated from 3-dimensional Discrete Anisotropic Radiative Transfer (DART) model to classify fuel types using spectral matching algorithms,” GIScience Remote Sens. **56**(7), 988–1023, Taylor & Francis (2019) [doi:10.1080/15481603.2019.1601805].

45. A. L. . Montealegre et al., “Multispectral and ALS data combination for fuel types mapping to support forest fire prevention planning,” in Sensors, Multi-Sensor Integration, Large Volumes: New opportunities and Challenges in Forest Fire Research, K. Themistocleous et al., Eds., p. 14, EARSeL, Limassol (2015).

46. F. Montealegre, A.L.; Lamelas, M.T.; García-Martín, A.; de la Riva, J. and Escribano, “Cartografía de Modelos de Combustible Mediante Combinación de Imágenes LiDAR, SAR y Ópticas en el Centro de Adiestramiento ‘San Gregorio,’” in III Congreso Nacional de i+d en Defensa y Seguridad, J. M. Asorey, R., Devesa, R., Solla, M.M., Pousada, Ed., pp. 1185–1192, University of Vigo, Vigo (2015).

47. F. Montealegre, A.L., Lamelas, M.T., García-Martín, A., de la Riva, J., Escribano, “Metodología para la caracterización de combustibles forestales mediante técnicas de teledetección y trabajo de campo,” in Los estudios militares y de seguridad en los albores del siglo XXI (Vol. II), R. Durán Cenit, M. y González Abellán, Ed., pp. 571–588, Universidad de Granada, Granada (2017).

48. M. Ruiz, L.A., Recio, J.A., Crespo-Peremarch, P., Sapena, “An object-based approach for mapping forest structural types based on low-density LiDAR and multispectral imagery,” Geocarto Int. **33**, 443–457 (2018) [doi:10.1080/10106049.2016.1265595].

49. Y. Sánchez Sánchez et al., “Mapping wildfire ignition probability using sentinel 2 and LiDAR (Jerte Valley, Cáceres, Spain),” Sensors (Switzerland) **18**(3), 1–18 (2018) [doi:10.3390/s18030826].

50. A. Ashworth et al., “Predicting southeastern forest canopy heights and fire fuel models using GLAS data,” Photogramm. Eng. Remote Sensing **76**(8), 915–922 (2010) [doi:10.14358/PERS.76.8.915].

51. R. Hoffrén et al., “Assessing GEDI-NASA system for forest fuels classification using machine learning techniques,” Int. J. Appl. Earth Obs. Geoinf. **116**, Elsevier B.V. (2023) [doi:10.1016/j.jag.2022.103175].

52. J. Hoffrén, R.; Lamelas, M.T.; de la Riva, “Classification and Mapping of Fuels in Mediterranean

Forest Landscapes Using a UAV-LiDAR System and Integration Possibilities with Handheld Mobile Laser Scanner Systems," Remote Sens. **16**, 3536 (2024) [doi:https://doi.org/10.3390/rs16183536].

53. S. Sinha et al., "A review of radar remote sensing for biomass estimation," Int. J. Environ. Sci. Technol. **12**(5), 1779–1792 (2015) [doi:10.1007/s13762-015-0750-0].
54. M. Santoro and O. Cartus, "Research pathways of forest above-ground biomass estimation based on SAR backscatter and interferometric SAR observations," Remote Sens. **10**(4) (2018) [doi:10.3390/rs10040608].
55. S. Englhart, V. Keuck, and F. Siegert, "Aboveground biomass retrieval in tropical forests - The potential of combined X- and L-band SAR data use," Remote Sens. Environ. **115**(5), 1260–1271, Elsevier Inc. (2011) [doi:10.1016/j.rse.2011.01.008].
56. F. Capodici, G. D'Urso, and A. Maltese, "Investigating the relationship between x-band SAR data from COSMO-skymed satellite and NDVI for LAI detection," Remote Sens. **5**(3), 1389–1404 (2013) [doi:10.3390/rs5031389].
57. Y. Duguay et al., "Potential of C and X band SAR for shrub growth monitoring in sub-arctic environments," Remote Sens. **7**(7), 9410–9430 (2015) [doi:10.3390/rs70709410].
58. R. Hagensieker and B. Waske, "Evaluation of multi-frequency SAR images for tropical land cover mapping," Remote Sens. **10**(2) (2018) [doi:10.3390/rs10020257].
59. M. Santoro et al., "Complementarity of X-, C-, and L-band SAR backscatter observations to retrieve forest stem volume in boreal forest," Remote Sens. **11**(13) (2019) [doi:10.3390/rs11131563].
60. C. Schuster et al., "Grassland habitat mapping by intra-annual time series analysis -Comparison of RapidEye and TerraSAR-X satellite data," Int. J. Appl. Earth Obs. Geoinf. **34**(1), 25–34, Elsevier B.V. (2015) [doi:10.1016/j.jag.2014.06.004].
61. H. J. Persson et al., "Experiences from large-scale forest mapping of Sweden using TanDEM-X data," Remote Sens. **9**(12) (2017) [doi:10.3390/rs9121253].
62. N. C. Gonzalez Bonilla, M. J.; Cuerda Munoz, J. M.; Carrasco, E. V. ; Rodriguez M. G. ; Vazquez, "PAZ Mission. Science Activities," in EUSAR 2021; 13th European Conference on Synthetic Aperture Radar, pp. 110–113, Verlag GMBD, Berlin (2021).
63. M. González Bonilla, M.J.; Cuerda Muñoz, J.M.; García Rodríguez, "PAZ Product definition procedure," in EUSAR 2018; 12th European Conference on Synthetic Aperture Radar, pp. 892–895, Verlag GMBD, Aachen (2018).
64. M. J. . González Bonilla et al., "Explotación científica de la misión paz anuncio de oportunidad: lanzamiento de la fase científica de PAZ (PAZ/INT/CALVAL/AO/001)," Madrid (2019).

65. D. Small, “Flattening gamma: Radiometric terrain correction for SAR imagery,” IEEE Trans. Geosci. Remote Sens. **49**(8), 3081–3093, IEEE (2011) [doi:10.1109/TGRS.2011.2120616].

66. S. Quegan and J. J. Yu, “Filtering of multichannel SAR images,” IEEE Trans. Geosci. Remote Sens. **39**(11), 2373–2379 (2001) [doi:10.1109/36.964973].

67. C. . Oliver and S. Quegan, *Understanding synthetic aperture radar images*, SciTech Publishing (2004).

68. D. H. . Ogle et al., “FSA: Simple Fisheries Stock Assessment Methods” (2025) [doi:10.32614/CRAN].

69. D. W. . Hosmer, S. . Lemeshow, and R. X. . Sturdivant, *Applied logistic regression*, John Wiley & Sons (2013).

70. T. . Hastie, R. . Tibshirani, and J. . Friedman, *The elements of statistical learning: Data mining, inference, and prediction*, Springer-Verlag (2009).

71. T. Van Der Ploeg, P. C. Austin, and E. W. Steyerberg, “Modern modelling techniques are data hungry: A simulation study for predicting dichotomous endpoints,” BMC Med. Res. Methodol. **14**(1), 1–13 (2014) [doi:10.1186/1471-2288-14-137].

72. W. N. . Venables and B. D. . Ripley, *Modern Applied Statistics with S*, Springer, New York (2002).

73. C. H. Van Essen, D.C.; Drury, H.A.; Dickson, J.; Harwell, J.; Hanlon, D.; Anderson, “An integrated software suite for surface-based analyses of cerebral cortex,” J. Am. Med. Inform. Assoc. **8**, 443–459 (2001).

74. P. J. Gelabert et al., “Forest structural diversity characterization in Mediterranean landscapes affected by fires using Airborne Laser Scanning data,” GIScience Remote Sens. **57**(4), 497–509, Taylor & Francis (2020) [doi:10.1080/15481603.2020.1738060].

75. E. Aragoneses and E. Chuvieco, “Generation and mapping of fuel types for fire risk assessment,” Fire **4**(3) (2021) [doi:10.3390/fire4030059].

76. A. Chhabra et al., “RADAR-Vegetation Structural Perpendicular Index (R-VSPI) for the Quantification of Wildfire Impact and Post-Fire Vegetation Recovery,” Remote Sens. **14**(13), 1–18 (2022) [doi:10.3390/rs14133132].

77. C. Wang et al., “Interpretable Multi-Sensor Fusion of Optical and SAR Data for GEDI-Based Canopy Height Mapping in Southeastern North Carolina,” Remote Sens. **17**(9) (2025) [doi:10.3390/rs17091536].

78. O. Cartus, M. Santoro, and J. Kellndorfer, “Mapping forest aboveground biomass in the Northeastern United States with ALOS PALSAR dual-polarization L-band,” Remote Sens. Environ. **124**, 466–478, Elsevier Inc. (2012) [doi:10.1016/j.rse.2012.05.029].

79. P. Ferrazzoli et al., “The potential of multifrequency polarimetric sar in assessing agricultural and arboreous biomass,” IEEE Trans. Geosci. Remote Sens. **35**(1), 5–17 (1997) [doi:10.1109/36.551929].

80. P. N. Bernardino et al., “Estimating vegetation water content from Sentinel-1 C-band SAR data over savanna and grassland ecosystems,” Environ. Res. Lett. **19**(3) (2024) [doi:10.1088/1748-9326/ad288f].

81. P. K. Srivastava et al., “Evaluation of radar vegetation indices for vegetation water content estimation using data from a ground-based SMAP simulator,” Int. Geosci. Remote Sens. Symp. **2015-Novem**, 1296–1299, IEEE (2015) [doi:10.1109/IGARSS.2015.7326012].

82. K. Wessels et al., “Quantifying the sensitivity of L-Band SAR to a decade of vegetation structure changes in savannas,” Remote Sens. Environ. **284**(August 2022), 113369, Elsevier Inc. (2023) [doi:10.1016/j.rse.2022.113369].

83. C. M. Ryan et al., “Quantifying small-scale deforestation and forest degradation in African woodlands using radar imagery,” Glob. Chang. Biol. **18**(1), 243–257 (2012) [doi:10.1111/j.1365-2486.2011.02551.x].

84. M. Tanase et al., “Sensitivity of SAR data to post-fire forest regrowth in Mediterranean and boreal forests,” Remote Sens. Environ. **115**(8), 2075–2085, Elsevier Inc. (2011) [doi:10.1016/j.rse.2011.04.009].

85. M. El Hajj et al., “Irrigated grassland monitoring using a time series of TerraSAR-X and COSMO-SkyMed X-Band SAR data,” Remote Sens. **6**(10), 10002–10032 (2014) [doi:10.3390/rs61010002].

86. S. Erasmi et al., “Sensitivity of bistatic TanDEM-X data to stand structural parameters in temperate forests,” Remote Sens. **11**(24), 1–18 (2019) [doi:10.3390/rs11242966].

87. J. Zhu et al., “High-resolution sub-canopy topography mapping via TanDEM-X DEM combined with future P-band BIOMASS PolInSAR data,” J. Geod. **97**(12), 1–21, Springer Berlin Heidelberg (2023) [doi:10.1007/s00190-023-01807-0].

88. C. Shen et al., “Research on forest height inversion algorithm based on X-band SAR data,” in International Conference on Precision Instruments and Optical Engineering, p. 12585 (2023) [doi:https://doi.org/10.1117/12.2667940].

89. J. M. Fernández-Guisuraga et al., “Estimation of Prometheus fuel types using physically based remote sensing techniques,” Fire Ecol. **21**(1), Springer International Publishing (2025) [doi:10.1186/s42408-025-00373-4].

90. S. Arellano-Pérez et al., “Potential of Sentinel-2A data to model surface and canopy fuel characteristics in relation to crown fire hazard,” Remote Sens. **10**(10) (2018)

[doi:10.3390/rs10101645].

91. Y. Hu et al., “Estimating forest stock volume in Hunan Province, China, by integrating in situ plot data, Sentinel-2 images, and linear and machine learning regression models,” Remote Sens. **12**(1) (2020) [doi:10.3390/RS12010186].

92. D. Domingo et al., “Quantifying forest residual biomass in Pinus halepensis Miller stands using Airborne Laser Scanning data,” GIScience Remote Sens. **56**(8), 1210–1232 (2019) [doi:10.1080/15481603.2019.1641653].

93. D. Domingo et al., “Temporal transferability of pine forest attributes modeling using low-density airborne laser scanning data,” Remote Sens. **11**(3) (2019) [doi:10.3390/rs11030261].

First Author is an Associate Professor at the University Center of Defense at the General Military Academy of Spain and an Honorary Fellow at the University of Zaragoza. He holds B.S.. M.S.. and Ph.D. degrees from the University of Zaragoza in Geography (2001). Geographic Information Technologies (2004). and Land Management and Environment (2009). respectively. He has authored more than 25 JCR papers and 10 book chapters. and has delivered numerous contributions at international and national conferences. His current research focuses on the estimation of continuous forestry parameters and the analysis of forest fires. specializing in fuel modeling. burn severity. and plant regeneration using remote sensing. Geographic Information Systems (GIS). and fieldwork.

Caption List

Table 4 Results from Kruskal-Wallis test for DVC and Prometheus FT. All variables were statistically significant (p-value < 0.05).

Table 5 Results from Dunn's test to distinguish categories DVC and Prometheus fuel types. All pairwise comparisons between the categories were statistically significant ($p < 0.05$).

Table 6 Confusion matrix and per-class accuracy metrics from the multinomial logistic regression model for the Dominant Vegetation Cover (DVC) classification. The results were obtained on the independent test dataset (n=28).

Table 7 Confusion matrix and per-class accuracy metrics from the multinomial logistic regression model for the Prometheus classification. The results were obtained on the independent test dataset (n=28).